PNAS RESEARCH ARTICLE | CHEMISTRY

# A tale of two topological isomers: Uptuning $[Fe^{IV}(O)(Me_4cyclam)]^{2+}$ for olefin epoxidation

Bittu Chandra[a], Faiza Ahsan[b], Yuan Sheng[a], Marcel Swart[b,c,1], and Lawrence Que Jr.[a,1]

Contributed by Lawrence Que; received November 15, 2023; accepted January 30, 2024; reviewed by Andrew S. Borovik, David P. Goldberg, and John T. Groves

**TMC-*anti* and TMC-*syn*, the two topological isomers of $[Fe^{IV}(O)(TMC)(CH_3CN)]^{2+}$ (TMC = 1,4,8,11-tetramethyl-1,4,8,11-tetraazacyclotetradecane, or $Me_4$cyclam), differ in the orientations of their $Fe^{IV}$=O units relative to the four methyl groups of the TMC ligand framework. The $Fe^{IV}$=O unit of TMC-*anti* points away from the four methyl groups, while that of TMC-*syn* is surrounded by the methyl groups, resulting in differences in their oxidative reactivities. TMC-*syn* reacts with HAT (hydrogen atom transfer) substrates at 1.3- to 3-fold faster rates than TMC-*anti*, but the reactivity difference increases dramatically in oxygen-atom transfer reactions. $R_2S$ substrates are oxidized into $R_2S$=O products at rates 2-to-3 orders of magnitude faster by TMC-*syn* than TMC-*anti*. Even more remarkably, TMC-*syn* epoxidizes all the olefin substrates in this study, while TMC-*anti* reacts only with *cis*-cyclooctene but at a 100-fold slower rate. Comprehensive quantum chemical calculations have uncovered the key factors governing such reactivity differences found between these two topological isomers.**

nonheme iron(IV)-oxo complexes | topological isomers | olefin epoxidation | tetramethylcyclam

Oxoiron(IV) species are key intermediates in biological and abiological oxidations like C–H hydroxylation and halogenation, as well as olefin epoxidation (1–4). A significant effort by various groups has led to the characterization of synthetic nonheme oxoiron(IV) complexes that serve as spectroscopic and functional mimics of nonheme iron oxygenases to enhance our understanding of these natural processes (4). Thus far, over a hundred such synthetic nonheme oxoiron(IV) complexes have been documented since the report of the crystal structure of *anti*-$[Fe^{IV}(O)(TMC)(CH_3CN)]^{2+}$ (TMC = 1,4,8,11-tetramethyl-1,4,8,11-tetraazacyclotetradecane, or $Me_4$cyclam), the first example for an oxoiron(IV) complex in a nonheme ligand environment (5). Much effort has since been invested in increasing our understanding of HAT (hydrogen-atom transfer) reactions that result in the hydroxylation of C–H bonds (6). However, much less attention has thus far been paid to OAT (oxygen-atom transfer) reactions, although some examples of olefin epoxidation have been reported for a handful of nonheme iron enzymes (7–9). Similarly, only a few examples of synthetic nonheme oxoiron(IV)-mediated epoxidation reactions have thus far been reported (10–14). In this article, we have explored the HAT and OAT reactivity of the *anti*- and *syn*-isomers of $[Fe^{IV}(O)(TMC)(CH_3CN)]^{2+}$ (Fig. 1) and find significantly faster OAT rates for $R_2S$ oxidation and olefin epoxidation by the *syn* complex relative to its *anti*-counterpart. Ligand topology would thus appear to be a critical factor in enhancing such oxidative reactivity, and our insights are reported in this paper.

## Results and Discussion

Oxoiron(IV) complexes supported by the TMC macrocycle can be generated as two discrete forms in $CH_3CN$, namely *anti*-, and *syn*-isomers, as determined by the orientation of the $Fe^{IV}$=O moiety relative to the four methyl groups on the macrocycle. TMC-*anti* or *anti*-$[Fe^{IV}(O)(TMC)(CH_3CN)]^{2+}$, reported in 2003, represents the first nonheme oxoiron(IV) complex to have been crystallographically characterized (5). It is formed by the reaction of $[Fe^{II}(TMC)(OTf)](OTf)$ with PhIO in $CH_3CN$. Its Fe=O unit points in the direction opposite to that of the four methyl groups of the TMC ligand, which surround the sixth ligand, namely $CH_3CN$. Twelve years later the corresponding TMC-*syn* isomer was obtained by using the sterically bulkier 2-$^t$Bu$SO_2$-$C_6H_4$IO (*s*-ArIO) oxidant, resulting in the $Fe^{IV}$=O unit pointing in the opposite direction and surrounded by the four methyl groups (15).While it is not yet fully understood why different topological isomers TMC-*anti* and TMC-*syn* are generated with PhIO and *s*-ArIO, respectively, it is clear that they are formed using these two distinct oxidants. When the $Fe^{II}(TMC)(OTf)_2$ precursor is reacted with PhIO, the only product isolated is the TMC-*anti* isomer, which is shown by XRD to adopt the *trans*-I (R,S,R,S) configuration with all four methyl groups

## Significance

The distinct oxidative reactivities reported here for the TMC-*anti* and TMC-*syn* isomers are surprising and require the examination of what factors can give rise to such differences for this class of iron complexes. In particular, our observation that the oxygen atom transfer reactivity of a nonheme $Fe^{IV}$=O unit can be so significantly enhanced by a simple flip in its orientation relative to its macrocyclic tetraamine host is truly remarkable and suggests that there is much more that can be learned for catalyst design by paying attention to the effect of ligand topology on the iron active site.

Author affiliations: [a]Department of Chemistry, University of Minnesota, Minneapolis, MN 55455; [b]Institut de Química Computacional i Catàlisi and Department of Chemistry, University of Girona, 17003 Girona, Spain; and [c]ICREA, 08010 Barcelona, Spain

Author contributions: B.C., M.S., and L.Q. designed research; B.C., F.A., and Y.S. performed research; B.C., F.A., Y.S., M.S., and L.Q. analyzed data; and B.C., F.A., M.S., and L.Q. wrote the paper.

Reviewers: A.S.B., University of California Irvine; D.P.G., Johns Hopkins University; and J.T.G., Princeton University.

The authors declare no competing interest.



[1]To whom correspondence may be addressed. Email: marcel.swart@gmail.com or larryque@umn.edu.

This article contains supporting information online at https://www.pnas.org/lookup/suppl/doi:10.1073/pnas.2319799121/-/DCSupplemental.

Published March 13, 2024.

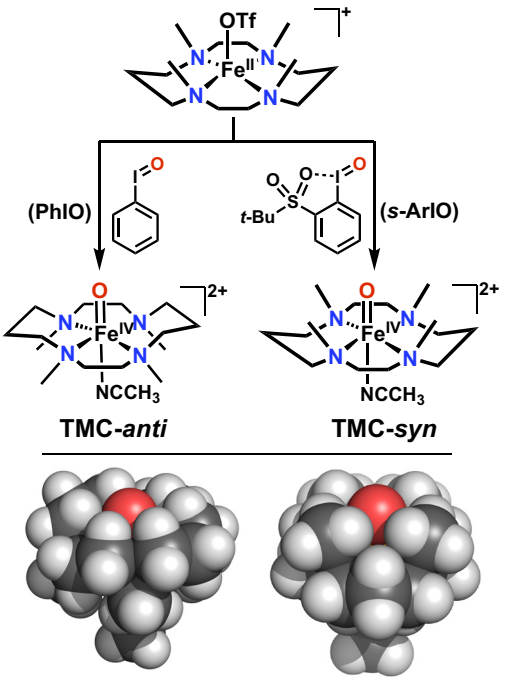


**Fig. 1.** *Top*: Generation of *anti* and *syn*-isomers of $[Fe^{IV}(O)(TMC)(CH_3CN)]^{2+}$ complexes in $CH_3CN$ by respective treatment of the $Fe^{II}$ precursor with oxo-transfer agents PhIO and the sterically bulkier s-ArIO at 25 °C. *Bottom*: van der Waals radii space-filling models for the *anti* (*Left*) and *syn* (*Right*) isomers showing greater substrate accessibility to the oxo atom in the *syn* isomer.

arrayed on one side of the macrocycle and the oxo atom bound to the *anti*-face of the TMC ligand (5). On the other hand, when $Fe^{II}(TMC)(OTf)_2$ is reacted with *s*-ArIO, an attack occurs at the less hindered *syn*-face to give TMC-*syn* (15). These observations show that the two isomers are formed by clearly distinct pathways with very little cross-contamination of the other isomer if at all. [Note: A complex we originally reported to be the TMC-*syn* isomer in 2008 (16) was later deduced to be the fluoride derivative of TMC-*anti* (15)].

A triflate anion has been found to be bound *trans* to the oxo atom in the crystal structure of TMC-*syn* (*SI Appendix*, Fig. S2). However, it is displaced by $CH_3CN$ upon dissolution into the solvent, as confirmed by its $^{19}$F-NMR spectrum showing a free triflate peak at ~79 ppm (*SI Appendix*, Fig. S3). Despite their structural differences, the two isomers exhibit quite similar UV-Vis and Raman features (Table 1) but give rise to distinct $^1$H-NMR spectra with paramagnetically shifted ligand resonances that are opposite in sign for the corresponding ligand protons in the two isomers (*SI Appendix*, Fig. S2), reflecting the opposite orientations of the paramagnetic Fe=O unit relative to the TMC macrocycle (15).

### H-Atom Transfer Reactivity Differences between TMC-*anti* and TMC-*syn* Isomers.

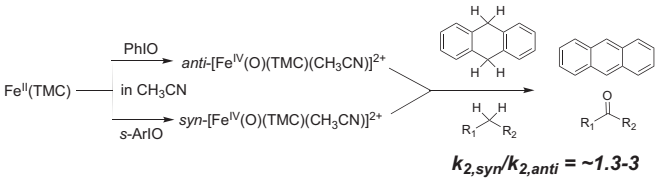


Perhaps not too surprisingly, the structural differences between the TMC-*anti* and TMC-*syn* isomers give rise to distinct HAT (H-atom transfer) and OAT (O-atom transfer) reactivity. As C–H bond cleavage is the reaction most commonly catalyzed by nonheme iron enzymes, earlier studies on synthetic nonheme $Fe^{IV}$=O complexes have focused mostly on HAT and the related concerted proton-coupled electron transfer (cPCET) reactions (17). Distinguishing between these two mechanisms can be done by inspection of the change in orbitals along the reaction path (18) or by computing the charge displacement function at the transition state (19). Here we used the latter approach to show (*SI Appendix*, Fig. S1) that the reactions studied here involve an HAT mechanism, and not cPCET. These studies compared TMC-*anti* with related complexes to assess relative rates of hydrocarbon oxidation that reveal a systematic decline in oxidation rates with an increase in C–H bond dissociation energy (3, 20). Parallel studies show that TMC-*syn* also exhibits a similar pattern of decreasing rates with substrates having stronger C–H bonds but at rates 1.3- to 3-fold higher than TMC-*anti* (Table 2 and *SI Appendix*, Fig. S5). Prior to doing these experiments, we had expected the methyl groups surrounding the Fe=O unit in TMC-*syn* to impose a greater steric barrier around the Fe=O unit and thus hinder the approach of the target substrate C–H bond to decrease its HAT reactivity. However, TMC-*syn* actually has an Fe–O bond 0.02 Å shorter than that of TMC-*anti* based on X-ray crystallography as well as a Raman Fe=O stretch that is 17 $cm^{-1}$ higher in frequency as observed in $CH_3CN$ solution (15) (Table 1). Both effects are corroborated by our DFT calculations at the B97-D3/TZ2P (21, 22) [COSMO (23–25), ZORA (26)] level, which show a 0.012 Å shorter Fe=O bond with a 28 $cm^{-1}$ higher Fe=O frequency (Table 1).

The higher rates for TMC-*syn* can be rationalized in part by the greater access of the substrate to the oxo atom on its Fe=O moiety

**Table 1. Experimental (and *DFT-derived*) properties of TMC-*anti* and TMC-*syn complexes***

| Properties | TMC-*anti* *S* = 1 | TMC-*anti* *S* = 2 (*DFT*) | TMC-*syn* *S* = 1 | TMC-*syn* *S* = 2 (*DFT*) |
|---|---|---|---|---|
| r(Fe–O) (Å) | 1.646 (*1.636*) | *1.633* | 1.625 (*1.624*) | *1.623* |
| r(Fe–$N_{ave}$) (Å) | 2.091 (*2.131*) | *2.220* | 2.068 (*2.123*) | *2.217* |
| r(Fe–L) (Å) | 2.058 (*2.026*) | *2.012* | 2.146 (*2.093*) | *2.076* |
| r(Fe-oop)* (Å) | **−0.033** (*−0.027*) | *−0.026* | **+0.063** (*+0.106*) | *+0.155* |
| $\lambda_{max}$ (nm) | 825 (*706*) | *608* | 815 (*691*) | *604* |
| $\nu$ (Fe=O) ($cm^{-1}$) | 839 (*864*) | *877* | 856 (*892*) | *903* |
| $\delta$ (mm $s^{-1}$) | 0.17 (*0.152*) | *0.143* | 0.16 (*0.149*) | *0.149* |
| $\Delta E_Q$ (mm $s^{-1}$) | 1.24 (*0.962*) | *−0.948* | 1.55 (*1.274*) | *−0.599* |

*Fe-oop = out-of-plane distance between the Fe and the plane defined by the four TMC-N atoms (see *SI Appendix, Computational Details*, for information on how these values were obtained). Note that all the italicized texts in this table represent results from DFT calculations.

**Table 2. Comparison of TMC-*anti*/TMC-*syn* HAT and OAT rates [$k_2$ ($M^{-1}s^{-1}$) at 25 °C]**

| Substate | TMC-*anti* | TMC-*syn* | *syn/anti* | *Products (yield)* |
|---|---|---|---|---|
| **HAT** | | | | |
| Xanthene | 0.67 | 0.92 | 1.4 | Xanthone (1.0) |
| 9,10-DHA | 0.23 | 0.33 | 1.5 | Anthracene (0.56) |
| 1,4-CHD | 0.22 | 0.29 | 1.3 | Benzene (0.52) |
| Fluorene | 0.01 | 0.02 | 2 | Fluorenone (0.60) |
| Cyclohexene | 0.002 | 0.006 | 3 | Cyclohexenol (0.70) |
| **OAT ($R_2S$)** | | | | |
| c-$C_4H_8S$ | 0.14 | 19 | 135 | *1*-$C_4H_8S(O)$ (0.33) |
| $Me_2S$ | 0.097 | 13 | 135 | $Me_2S(O)$ (0.45) |
| PhSMe | 0.0096 | 8.2 | 855 | PhS(O)Me (0.50) |
| $Ph_2S$ | N. R. | 0.96 | extreme | $Ph_2S(O)$ (0.63) |

Reaction conditions: 1.0 mM [$Fe^{II}$(TMC)(OTf)](OTf) in $CH_3CN$, 1.5 mM PhIO/s-ArIO, and >100 mM substrate reacted under Ar at 25 °C. N. R. denotes no reaction under these conditions.

relative to that of the corresponding TMC-*anti* due to its larger out-of-plane distance (Fe-oop) relative to the plane spanned by the equatorial nitrogen atoms of the TMC macrocycle (Table 1). For TMC-*anti*, the iron center is found to be below the N4 plane (–0.03 Å, as shown by X-ray crystallography), moving closer to the axial acetonitrile ligand. In contrast for TMC-*syn*, the iron is found to be above the N4 plane (+0.06 Å, observed by X-ray crystallography), moving away from the acetonitrile, thereby increasing the exposure of the oxo atom (Fig. 1, *Bottom*) and enhancing its oxidative reactivity. In fact, the van der Waals radii space-filling model in Fig. 1 (*SI Appendix*, Fig. S14) shows the oxo atom of TMC-*syn* to be actually more accessible to the substrate, as the $CH_3$ groups are in fact more spread out in space. In contrast, the oxo atom of TMC-*anti* is surrounded by well-packed H-atoms that make it less accessible (Fig. 1, *Bottom*, and *SI Appendix*, Fig. S14). We have estimated the exposed surface area with the Connolly surface area approach (27) and indeed observed a slightly larger area of the oxo atom that is exposed in TMC-*syn* (33.44 $Å^2$) than in TMC-*anti* (31.33 $Å^2$).

We have investigated the HAT reactions with 9,10-dihydroanthracene (DHA) and cyclohexene (*c*-$C_6H_{10}$) using DFT calculations at the B97-D3/TZ2P level to shed light on the higher reactivity observed experimentally for TMC-*syn* relative to TMC-*anti*. Note that we have designated the corresponding barriers with respect to the $S = 1$ reactant complex, which is the spin ground state of the reactants. Subsequently, we observe the usual involvement of the σ-reaction channel (28–30) and two-state reactivity (31–33) (Scheme 1) whereby the reaction starts on the $S = 1$ surface and then switches over to the $S = 2$ surface further along on the reaction coordinate, as the latter has a lower barrier (*SI Appendix*, Fig. S17).

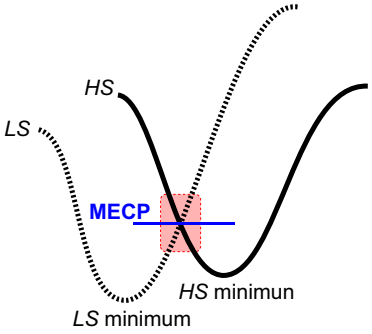


**Scheme 1.** Switching between two spin states in the two-state reactivity model (LS is low spin, and HS is high spin), with the switching region shown in red; the energy of the minimum-energy crossing point (MECP) is indicated by the horizontal line.

Apart from the structural changes surrounding the Fe(IV)=O reactant leading to its larger exposure during the reaction pathway (vide supra), we find yet another aspect of the TMC-*syn* complex that contributes to its increased reactivity. At the transition state of the HAT reactions of TMC-*syn*, the Fe=O unit moves further out of the plane with respective Fe-oop distances of +0.22 Å and +0.25 Å (Fig. 2 and *SI Appendix*, Table S1). Interestingly, these differences already exist at the reactants stage in the $S = 2$ state, where the metal center is found to be 0.16 Å above the TMC-*syn* plane. So, this is clearly an effect of switching to the higher spin state at the transition state. At the same time, the axial acetonitrile moves away ca. 0.15 Å from the plane spanned by the TMC-*syn* ligand (Fig. 2), in the direction opposite from the Fe=O unit, resulting in the generation of a 5-coordinate Fe=O center.

In great contrast, the metal center in TMC-*anti* remains in the same position below the TMC-*anti* plane (ca. –0.03 Å) for both $S = 1$ and $S = 2$ species. Furthermore, the Fe=O unit for the HAT transition states with TMC-*anti* are found to move only slightly, by ca. +0.04 Å as compared to the *syn* counterpart (where it moved by 0.11 to 0.14 Å; see Fig. 2 and *SI Appendix*, Table S1). Similarly, the movement of acetonitrile at the TS (ca. 0.06 to 0.07 Å) in TMC-*anti* is smaller than observed in TMC-*syn* (0.07 to 0.10 Å, see *SI Appendix*, Table S1). Consequently, the slightly altered structures lead us to a relatively small reactivity difference (1.3- to 3-fold) between TMC-*syn* and TMC-*anti* for HAT reactions. To our great surprise, the difference in OAT rates observed for TMC-*anti* and TMC-*syn* are significantly larger, emphasizing distinctions in the mechanisms of these two transformations.

A compelling rationale for the out-of-plane movement of the axial $CH_3CN$ ligand and the consequent weakening of the axial ligand field for TMC-*syn* can be found by inspection of the frontier molecular orbitals (Fig. 3, *Top*). As previously noted (30, 34, 35), the $d_{xy}(\beta)$ acceptor orbital of the high-spin $S = 2$ complex is found to be at a lower energy than in its $S = 1$ analog, bringing it closer to the highest-occupied MO of the substrate. As a result, electron transfer from the substrate to the metal is facilitated, leading to a lower barrier. In the case of the TMC-*syn* reactant, this acceptor orbital is found to be 0.03 eV lower in energy than for TMC-*anti*, consistent with its higher HAT reactivity. Dissociation of the bound $CH_3CN$ would lower the energy of this orbital even further, but this would be accompanied by the loss of favorable metal–ligand bonding interactions. Hence, there is a subtle balance between

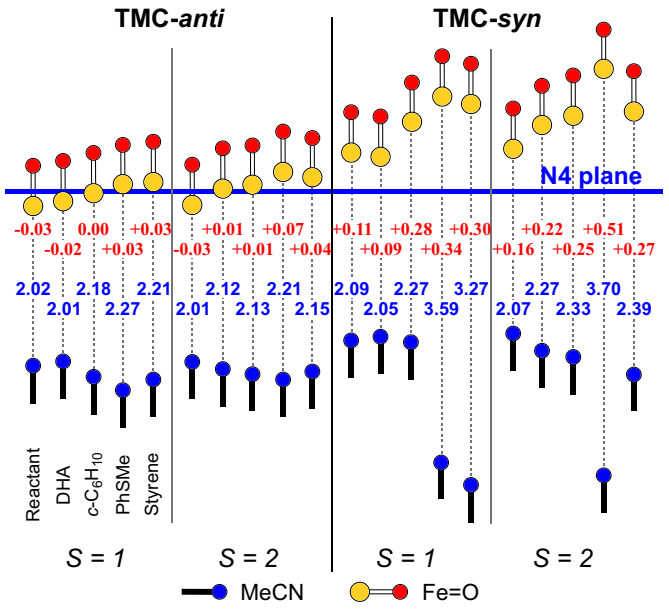


**Fig. 2.** Out-of-plane distances of the Fe=O and the $CH_3CN$ units relative to the N4 plane (B97-D3/TZ2P) for $S = 1$ and $S = 2$ states of TMC-*anti* and TMC-*syn*, for Fe=O reactants, and transition states of HAT (DHA, *c*-$C_6H_{10}$) and OAT (PhSMe, styrene) substrates. Shown with dotted lines are the distances between iron and the axial $CH_3CN$. Also indicated (in red, next to the Fe=O unit) are the Fe-oop distances.

lowering the acceptor orbital for enhanced electron transfer and the energetic penalty associated with it. Our results show that for HAT, the metal–ligand interactions are strong enough that only a mild dissociation of $CH_3CN$ takes place.

**OAT Reactivity Differences between TMC-*anti* and TMC-*syn* Isomers.**

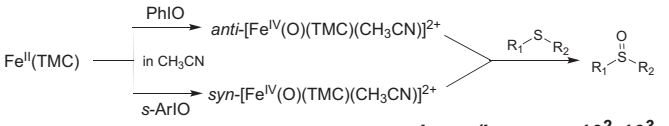


$k_{2,syn}/k_{2,anti}$ = ~$10^2$-$10^3$

***OAT to sulfides.*** More dramatic reactivity differences are observed between the *anti* and *syn* isomers in OAT transformations (Table 2). At 298 K, TMC-*syn* oxidizes dialkyl sulfides at rates ~130-fold faster than TMC-*anti*, a difference which grows to ~850-fold for alkyl aryl sulfides (Table 2 and *SI Appendix*, Fig. S6). This trend suggests that electronic factors play a much bigger role than steric considerations in controlling OAT reactivity (vide supra).

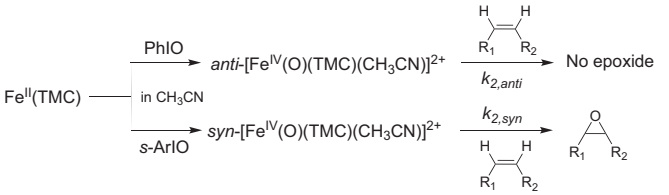


$k_{2,syn}/k_{2,anti}$ = extreme

***Olefin epoxidation.*** Extension of our reactivity explorations to olefin epoxidation reveals even further surprises. Quite intriguingly, we have observed the epoxidation of a series of olefins, but ***only*** by the TMC-*syn* isomer (Table 3). Indeed TMC-*anti* is essentially unreactive with the olefins we have tested, except for *cis*-cyclooctene, the most electron-rich olefin in our list, which is epoxidized by TMC-*anti* but at a rate 100-fold slower than the corresponding TMC-*syn* isomer. This comparison emphasizes the effectiveness of TMC-*syn* as an olefin epoxidation agent. As shown in Fig. 4, *Inset*, epoxidation rates span a range of two orders of magnitude, from $1.5 \times 10^{-3}$ $M^{-1}s^{-1}$ for 1-octene to 0.13 $M^{-1}s^{-1}$ for *trans*-stilbene, and in between is styrene with an intermediate rate of $1.6 \times 10^{-2}$ $M^{-1}s^{-1}$ that is further modulated by introducing substituents on the phenyl ring (Table 3 and *SI Appendix*, Fig. S7). Clearly, conjugation to the double bond lowers the barrier for epoxidation to enhance the reaction rate. Intriguingly, a linear correlation is obtained between the second-order rate constants (log $k_2$) vs. their 1-e oxidation potentials ($E_{ox}$) with a slope of –1.1 (Fig. 4, *Inset*), suggesting that epoxidation likely occurs in two steps: initial inner-sphere electron transfer from olefin to the Fe=O unit, followed by a radical rebound step. This hypothesis is supported by the partial *cis*-to-*trans* isomerization observed for the two open-chain *cis*-disubstituted olefins *cis*-2-heptene (*cis:trans* = 2.8:1) and *cis*-stilbene (*cis:trans* = 1:2), with the fraction of *trans* epoxide formed enhanced by the introduction of aromatic substituents that increase the lifetime of the 1-e-oxidized substrate. The correlation of the epoxidation rates to oxidation potentials of the olefin substrates is reminiscent of the observation of such a complex in olefin epoxidation by oxo-iron porphyrins (36).

Indeed, in our DFT study, we do find that the reaction proceeds through a two-step mechanism, following the σ-reaction channel (28–30) in which the oxo moiety binds to one of the carbons of the double bond in the first (inner-sphere electron transfer) step and then subsequently in the second step makes the bond to the second carbon to form the epoxide product. This result is in line with previous computational studies (40, 41) on OAT

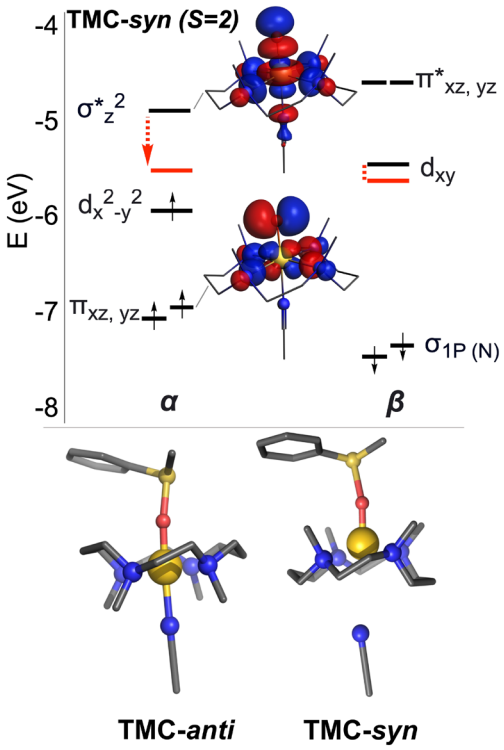


**Fig. 3.** *Top*: Energies of the frontier MOs for the $S = 2$ configuration of TMC-*syn*. Indicated in red is the decrease in the energy of the σ* and $d_{xy}$ orbitals upon lengthening of the Fe–$NCCH_3$ bond to 2.5 Å. Corresponding figures for $S = 1$ and $S = 2$ of TMC-*anti* can be found in *SI Appendix*, Fig. S16. *Bottom*: Transition state structures calculated for TMC-*anti* (*Left*) and TMC-*syn* (*Right*) in their reactions with PhSMe (H-atoms omitted for clarity) where the $CH_3CN$ ligand becomes detached from the Fe center upon reaction of TMC-*syn* with substrate, but NOT in the case of TMC-*anti*.

**Table 3. Olefin epoxidation rates and yields for nonheme $Fe^{IV}$=O complexes, at 25 °C unless otherwise noted**

| Fe=O Complex | $k_2$ ($M^{-1}s^{-1}$) | Epoxide yield |
|---|---|---|
| **TMC-*syn* *(this work)*** | | |
| 1-octene | 0.0015 | 0.32 |
| *trans*-4-octene | 0.005 | 0.36 |
| *trans*-2-heptene | 0.009 | 0.29 |
| *cis*-2-heptene | 0.013 | 0.38 (*cis:trans* 2.8:1) |
| *cis*-cyclooctene | 0.014 | 0.70 |
| styrene | 0.016 | 0.38 |
| 4-Me-styrene | 0.03 | 0.45 |
| 4-MeO-styrene | 0.08 | 0.50 |
| 4-Cl-styrene | 0.007 | 0.21 |
| *cis*-stilbene | 0.011 | 0.41 (*cis:trans* 1:2) |
| *trans*-stilbene | 0.13 | 0.45 |
| **$[Fe^{IV}(O)(PyMAC)]^{2+}$*** | | |
| Cyclooctene | 0.45 | 0.81 |
| **$[Fe^{IV}(O)(N3S2)]^{2+}$†** | | |
| Styrene | 0.026 | 0.60 |
| **$[Fe^{IV}(O)(N2Py2Q)]^{2+}$‡** | | |
| 4-X-styrenes | 0.186 to 2.53 | |
| *cis*-stilbene | 0.139 | |
| *trans*-stilbene | 1.12 | |
| **$[Fe^{IV}(O)(cyclam)]^{2+}$§** | **at −20 °C** | |
| 1-octene | 0.013 | 0.33 |
| cyclohexene | 0.015 | 0.60 |
| *cis*-stilbene | 0.023 | 0.30 |
| **$[Fe^{IV}(O)(Me_3NTB)]^{2+}$¶** | **at −40 °C** | |
| 4-X-styrenes | 5.8 to 29 | 0.89 (for styrene) |
| **$[Fe^{IV}(O)(TQA)]^{2+}$#** | **at −40 °C** | |
| Cyclooctene | 3.3 | 0.55 |
| 1-octene | 5.3 | 0.35 |
| 4-X-styrenes | 1.4 to 12 | 0.92 (for styrene) |

Ligand abbreviations: PyMAC = 2,7,12-trimethyl-3,7,11,17-tetraaza-bicyclo[11.3.1]-heptadeca-1(17),13,15-triene, N3S2 = 2,6-bis(2-methylthiophenylimino-methyl)pyridine, N2Py2Q = bis(pyridyl)methyl bis(quinolylmethyl)amine, $Me_3NTB$ = tris((1-methyl-1H-benzo[d]imidazol-2yl)methyl)-amine, TQA = tris(quinolin-2-yl-methyl)amine.
*From ref. 12.
†From ref. 11.
‡From ref. 14.
§From ref. 37.
¶From ref. 13.
#From refs. 13 and 38. X = para substituents of styrene (–$OCH_3$, –$CH_3$, –H, –Cl, –$NO_2$).

mechanisms that showed such a two-step mechanism for olefin epoxidation.

Interestingly, *cis*-stilbene is an order of magnitude less reactive than its *trans* counterpart, despite having an $E_{ox}$ value just higher by 0.2 V. Its significantly lower reactivity may result from the *cis* disposition of the two phenyl substituents on the double bond that may hinder the approach of the Fe=O moiety. Our DFT studies suggest this to be the case. The Ph–C=C–Ph dihedral angle for *trans*-stilbene (180° in substrate) changes relatively little at the TS (167.9° with TMC-*syn*, 155.5° with TMC-*anti*). Instead, for *cis*-stilbene (8° in substrate), it changes to 33.4° (TMC-*syn*) and 39.0° (TMC-*anti*) at the TS. Furthermore, our DFT calculations indicate that the first barrier in the mechanism is indeed lower for *trans*-stilbene with TMC-*syn* (ΔG 9.43 *trans*-stilbene vs. 10.52 kcal·$mol^{-1}$ *cis*-stilbene) (*SI Appendix*, Figs. S28 and S29). Moreover, *cis*-stilbene affords a mixture of *cis*- and *trans*-epoxide products with a ratio of 1:2 in favor of the *trans*-epoxide, suggesting that the proposed rebound step occurs more slowly in the case of this substrate. The only other *cis*-di-substituted-olefin in this study, namely *cis*-2-heptene, also yields a mixture of epoxide products, but with the *cis*-epoxide favored 2.8:1 over its *trans* counterpart. The difference in the two epoxidation results is likely correlated with the lifetime of the putative 1-e-oxidized olefin derivative, which should be longer for *cis*-stilbene due to the presence of phenyl groups that can conjugate with the 1e-oxidized olefin to extend the lifetime of the 1-e-oxidized radical cation intermediate. Indeed, according to our DFT calculations, the 1-e-oxidized intermediate is 10.8 kcal·$mol^{-1}$ more stable than the corresponding $S$ = 2 TS with *cis*-stilbene (with TMC-*syn*); in contrast, for *trans*-stilbene, the intermediate is located only 5.7 kcal·$mol^{-1}$ below the $S$ = 2 TS. At this intermediate, the Ph–C=C–Ph dihedral angle for *trans*-stilbene has lowered to 144.5° (i.e., a change of 36° compared to reactants), while for *cis*-stilbene it has increased to 53.4° (a change of 45° compared to reactants). In the latter case, a small rotational barrier (ca. 3.8 kcal·$mol^{-1}$ at electronic energy) might then easily move it over to the *trans*-stilbene orientation, leading to the *trans*-epoxide product. The second step in the process to epoxide has smaller barriers than the first step (7.6 kcal·$mol^{-1}$ for *cis*-stilbene, 5.9 kcal·$mol^{-1}$ for *trans*-stilbene), in which the bond between oxygen and the distal carbon is already partially formed (O–C *trans*-stilbene: 1.785 Å for TMC-*syn*, 1.895 Å for TMC-*anti*) (*SI Appendix*, Fig. S22).

***Hammett parameters.*** The OAT reactivity of the TMC-*syn* isomer has been further studied with a series of para-substituted thioanisoles and styrenes, showing that electron-donating substituents display enhanced second-order rate constants ($k_2$) compared to their electron-withdrawing counterparts (Tables 3 and 4). The ($k_2^X/k_2^H$) value was used for linear free energy correlation analysis (*SI Appendix*, Fig. S8) where $\log(k_2^X/k_2^H)$ values vs. $\sigma_\rho^+$ values of para-substituted thioanisoles and styrenes were plotted and Hammett ρ value of −1.3 for para-substituted thioanisoles and −2.0 for para-substituted styrenes were obtained. The relatively higher value of ρ indicated the buildup of a positive charge on the olefinic carbon in the transition state. Although we have not explicitly studied the para-substituted styrenes computationally, we did explore the buildup of charge on the olefinic carbons of styrene in going from the reaction complex

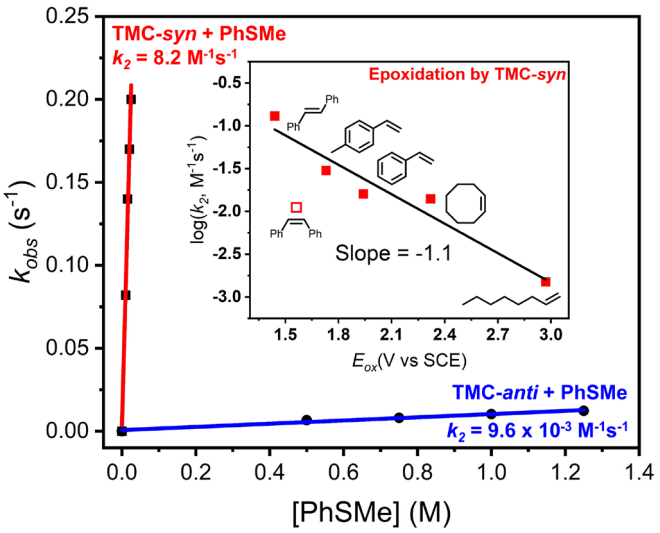


**Fig. 4.** PhSMe reaction rates with TMC-*syn* and TMC-*anti* observed at 25 °C. (*Inset*) Plot of log $k_2$ obtained at 25 °C vs. $E_{ox}$ of olefins with 1-e oxidation potentials from ref. 39.

**Table 4. Oxidative reactivity of oxoiron(IV) complex pairs with different topologies**

| Isomer pairs | Reactivity differences between isomers | Ref. |
|---|---|---|
| $[Fe^{IV}(O)(BQCN)(CH_3CN)]^{2+}$<br>***cis*-α > *cis*-β** (ΔE = 0.11 V) | HAT (cumene): 20x<br>OAT (p-CN-$C_6H_4$SMe): 100x | (43) |
| $[Fe^{IV}(O)(BP)]^{2+}$<br>**BP1 > BP2** (ΔE = 0.25 V) | HAT: 10 to 20x<br>OAT: sulfoxidation 100x | (44) |
| $Fe^{IV}(O)(\mathbf{Me_2EBC})(CH_3CN)]^{2+}$<br>**> TMC-*anti*** (ΔE = 0.06 V) | HAT: ~30 to 100x<br>OAT: sulfoxidation ~400x | (20) |
| $[Fe^{IV}(O)(TMC)(CH_3CN)]^{2+}$<br>**TMC-*syn* > TMC-*anti***<br>($E_{red}$ = 0.36 & 0.39 V vs. SCE @ 25 °C) | HAT: 1.5-3x<br>OAT: sulfoxidation 100-850x<br>cyclooctene epoxidation 100x<br>Epoxidation only by **TMC-*syn***: 1-octene, 4-R-styrene (R = H, Me, MeO, Cl) *trans*-stilbene (no *cis* epoxide product) *cis*-stilbene (1:2 *cis:trans* epoxide) | This work |

ChemDraw pictures for these complexes can be found in Fig. 5.

to the transition state. These data showed that for the proximal carbon (making a bond to oxo in the first step of the reaction) the MDC-d (42) charge increases along the pathway, from 0.07 e at the RC ($S$ = 1 and $S$ = 2) to 0.23 e at the TS ($S$ = 2). It is accompanied by creation of radical character on the substrate (*SI Appendix*, Fig. S20), which is located primarily on the distal olefin carbon atom of styrene (ca. 0.27 e), *cis/trans*-stilbene (ca. 0.27/0.31 e) and *cis*-cyclooctene (ca. 0.27 e). Moreover, for styrene and stilbene, a significant radical character is observed at the para-position of the phenyl group (ca. 0.09/0.10 e) that is bound to this distal carbon (*SI Appendix*, Fig. S20).

***Comparing with other topological isomeric pairs.*** Previously published work provides hints that ligand topology can play a role in modulating reactivity, as observed for two pairs of isomers among the nonheme oxoiron(IV) complexes (Table 4). In the first two pairs of isomers compared by Nam and Comba, the *cis*-α isomers are found $[Fe^{IV}(O)(BQCN)(CH_3CN)]^{2+}$ (BQCN = N,N′-dimethyl-N,N′-bis(8-quinolyl)-cyclohexanediamine) (with the quinoline rings-oriented *trans* to each other) to be more reactive than the *cis*-β counterparts (with the quinoline rings oriented *cis* to each other) by 10- to 20-fold with respect to HAT and 100-fold with respect to OAT (43). Similarly, Comba and coworkers have compared the reactivities of a second pair of complexes consisting of $[Fe^{IV}(O)(BP1)]^{2+}$ and $[Fe^{IV}(O)(BP2)]^{2+}$, (BP = 3,7-diazabicyclo[3.3.3]nonane), which also differ in the relative orientations of the two pyridine rings; the BP2 isomer with the two pyridine rings perpendicular to the Fe=O bond is more reactive by 20- to 40-fold (HAT) and 100-fold (OAT) than the BP1 isomer (44).

The reactivity differences within each pair of complexes can be qualitatively rationalized by differences in the $Fe^{IV/III}$ reduction potentials between the two members of each pair, 0.11 V for the BQCN pair and 0.25 V for the BP pair. In both cases, the isomer with the more positive reduction potential is the more reactive complex. On the other hand, two structurally related complexes $[Fe^{IV}(O)(Me_2EBC)(CH_3CN)]^{2+}$ ($Me_2EBC$ = 4,11-dimethyl-1,4,8,11-tetraazabicyclo-[6.6.2]hexadecane) and *anti*-$[Fe^{IV}(O)(TMC)(CH_3CN)]^{2+}$ exhibit large differences in reactivity (~50-fold for HAT and ~400-fold for OAT) despite having a small difference in $Fe^{IV/III}$ potentials (0.06 V). We also carried out cyclic voltammetry experiments to obtain $Fe^{IV/III}$ reduction potentials for TMC-*syn* and TMC-*anti* in $CH_3CN$ at 25 °C. Unfortunately, the resulted cyclic voltammograms are irreversible having one prominent cathodic peak with a small difference in $E_{p,c}$ values (33 mV) between them (*SI Appendix*, Fig. S9). When we performed spectral redox titrations using ferrocene the same difference was obtained (*SI Appendix*, Fig. S10). The $E_{red}$ value of TMC-*syn* was determined to be $E_{red}$ = 0.36 V vs. SCE at 25 °C. A value of 0.39 V vs. SCE was reported for

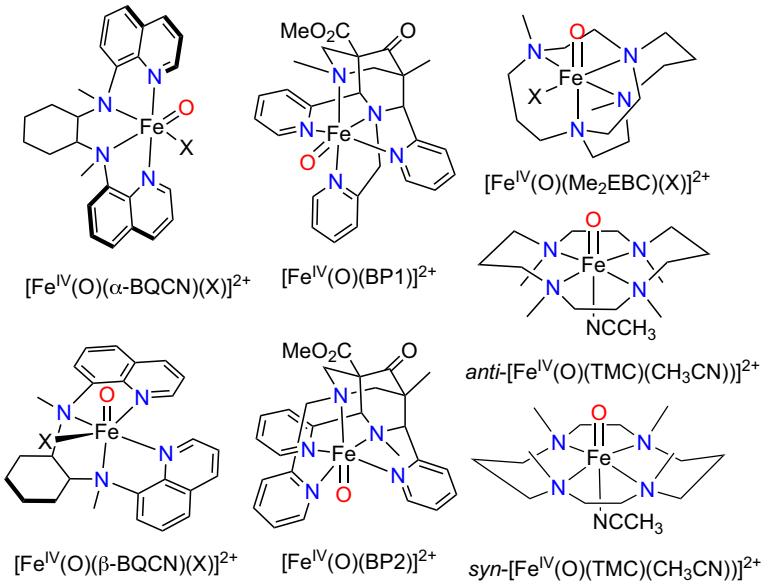


**Fig. 5.** Oxoiron(IV) complexes with different ligand topologies showing HAT and OAT reactivity differences.

TMC-*anti* at 25 °C (45). So, the difference in reduction potential is only 30 mV, a factor of 4-8-fold smaller than found the BQCN and BP pairs of complexes. So, it is difficult to apply the reduction potential argument to rationalize the observed reactivity difference.

**What Factors, Then, Are responsible for Extreme OAT Differences in Reactivity between TMC-*syn* and TMC-*anti*?** Our DFT calculations at B97-D3/TZ2P indicate that the higher reactivity of TMC-*syn* could partially be explained by the higher accessibility of its Fe=O unit. However, further examination of the transition states for the OAT reactions shows that more factors are involved in the higher reactivity of TMC-*syn*. In the case of OAT to thioanisole with TMC-*syn*, the Fe=O unit moves further out of the plane defined by the equatorial nitrogen atoms of TMC (Fig. 2). More importantly, the axial $CH_3CN$ dissociates from the Fe=O unit of TMC-*syn* in the transition state during OAT reactions, while it stays bound within TMC-*anti* (Fig. 2). We have explored this effect in more detail and performed constrained transition-state searches and geometry optimizations, in which we kept the Fe-N($CH_3CN$) distance fixed at 2.20 Å. These constrained TS searches increase the barrier for OAT with TMC-*syn* by ca. 6.3 kcal·mol$^{-1}$, which recovers part of the difference in barrier between TMC-*syn* and TMC-*anti* (11.0 kcal·mol$^{-1}$), but not completely. Apart from thioanisole oxidation, we also computed the reaction pathways with diphenyl sulfide and dimethyl sulfide. Our DFT results (*SI Appendix*, Table S2) corroborate the experimental values from Table 2 that show a decrease in reaction rates in the order $Me_2S$ > PhSMe > $Ph_2S$, reflecting an increase of the reaction barrier along this series. For PhSMe, the transition barrier ($\Delta G^{\ddagger}$) for TMC-*anti* is 15.7 kcal·mol$^{-1}$ at the $S$ = 2 spin state and is even higher for the $S$ = 1 spin state at 27.1 kcal·mol$^{-1}$ (in both cases with respect to the reactant complex in the $S$ = 1 state). On the other hand, the transition barriers for TMC-*syn* are 4.6 kcal·mol$^{-1}$ and 15.6 kcal·mol$^{-1}$ for the $S$ = 2 and $S$ = 1 spin states, respectively. However, for both TMC-*syn* and TMC-*anti*, a spin-state switching needs to go from the $S$ = 1 state at the reactant complex to the $S$ = 2 state at the TS. Therefore, we also located the minimum energy crossing points (MECP) (46–48), which are those points in space where the $S$ = 1 and $S$ = 2 states have the same electronic energy. In the case of TMC-*syn*, this MECP is found at +8.2 kcal·mol$^{-1}$ above the $S$ = 1 RC (and 1.7 kcal·mol$^{-1}$ below the corresponding $S$ = 2 TS). Hence, a major part of the barrier involves the spin barrier for switching over to $S$ = 2, and subsequently, only a small chemical barrier remains. Note that the chemical barrier for TMC-*anti* is considerably higher (vide supra), and the MECP to go from $S$ = 1 to $S$ = 2 is located well below it (+7.2 kcal·mol$^{-1}$ above the $S$ = 1 RC, and 13.7 kcal·mol$^{-1}$ below the corresponding $S$ = 2 TS) (*SI Appendix*, Fig. S19).

In the case of OAT for olefin substrates, the transition barrier is smallest (ca. 9.4 kcal·mol$^{-1}$) for the reaction of TMC-*syn* ($S$ = 2) with *trans*-stilbene, corresponding to the highest epoxidation rate observed. On the other hand, TMC-*anti* has a significantly higher transition barrier of 17.4 kcal·mol$^{-1}$. The experimental results show that TMC-*anti* is only reactive to *cis*-cyclooctene but at a much slower rate, which is corroborated by our DFT calculations that show the smallest barrier for this olefin (14.4 kcal·mol$^{-1}$) (*SI Appendix*, Fig. S21*C*). Nevertheless, it is still 2 to 5 kcal·mol$^{-1}$ larger than the corresponding barriers with TMC-*syn*. Our DFT study shows that the epoxidation of styrene is a two-step process involving two transition states. In the first step, the oxo attacks the proximal carbon, leading to a 1e-oxidized intermediate, which in the second step of the mechanism closes the epoxide ring (*SI Appendix*, Fig. S21*D*). The rate-determining step in all cases is the making of the C–O bond in the first step (9.4 kcal·mol$^{-1}$ for *trans*-stilbene), with the second step typically involving a barrier that is half as large (5.7 kcal·mol$^{-1}$ for *trans*-stilbene). An important aspect in this enhanced reactivity picture of TMC-*syn* is the axial acetonitrile, which detaches from iron during the reaction (Fig. 2).

**A Rationale For The Relationship Between The Axial Acetonitrile And Oxidative Reactivity.** The detachment of the acetonitrile takes place during OAT in the case of TMC-*syn*, but not with TMC-*anti*. We have estimated the effect of acetonitrile dissociation by performing constrained optimizations of TMC-*anti* and TMC-*syn*, where we increase the Fe–N($CH_3CN$) distance from 2.0 to 2.5 Å in steps of 0.1 Å. Interestingly, the $d_{xy}(\beta)$ orbital decreases in energy by only a small amount (from −5.52 eV to −5.66 eV for TMC-*syn*) as the axial acetonitrile distance increases from ca. 2.0 to 2.5 Å. More affected however is the $\sigma^*(\alpha)$ orbital, which drops by ca. 0.5 eV (from −4.9 eV to −5.4 eV). The combination of these two effects now allows us to propose a rationale for the effect of the orientation of the Fe=O unit within the TMC ligand (*anti* or *syn*) on reactivity. HAT reactions are one-electron processes, which involve the lower-lying $d_{xy}(\beta)$ orbital, so acetonitrile dissociation has only a limited effect on lowering of the orbital energy (and with it, increased overlap with

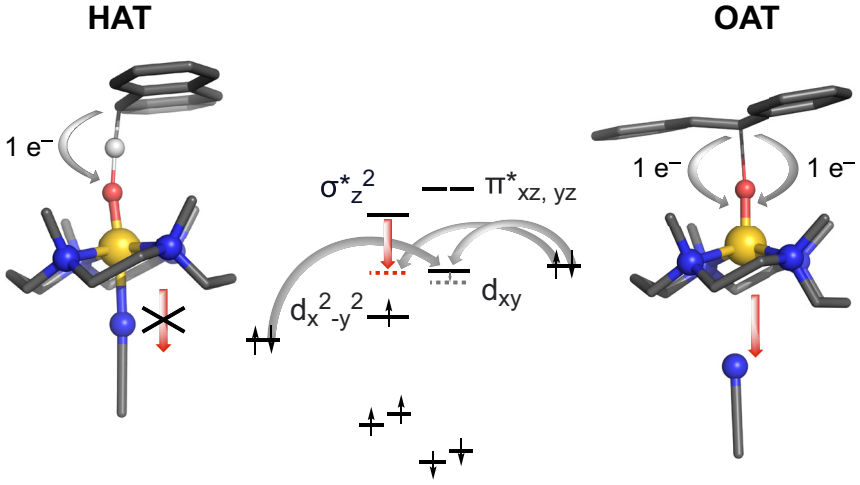


**Fig. 6.** Rationalizing the different outcomes found for the axial $CH_3CN$ of TMC-*syn* following the 1-e HAT reaction with DHA (*Left*) and the 2-e OAT reaction with *trans*-stilbene (*Right*), where $CH_3$ CN dissociation occurs only in the latter case. Shown in gray are the electron transfers from the substrate MOs to the Fe-complex MOs. A red arrow indicates the lowering of the σ* orbital, which facilitates the enhanced OAT reactivity for TMC-*syn*.

the substrate occupied orbital for more efficient electron transfer). Therefore, there is a limited amount of dissociation observed and relatively small effects on reaction rates (Fig. 6).

On the other hand, OAT reactions are two-electron processes that require involvement of the σ*(α) orbital, which is highly sensitive to the positioning of the $CH_3CN$ axial ligand, due to the occupation of the anti-bonding $d_z^2$ orbital on the metal center. The further the acetonitrile moves away from the Fe=O center, the lower the orbital energy of σ*(α), leading to the corresponding favorable effect on the reactivity in the $S = 2$ state. Indeed, we do see enhanced reactivity for OAT with TMC-*syn* that is accompanied by the gradual dissociation of the acetonitrile ligand. Although the lowering of the σ*(α) orbital is also seen for TMC-*anti*, the energetic cost for $CH_3CN$ dissociation is substantial, much more than for TMC-*syn*. This partial dissociation of the acetonitrile to a Fe–N($NCCH_3$) distance of 2.5 Å costs ca. 8.5 kcal·mol$^{-1}$ for TMC-*anti*, but only ca. 4 kcal·mol$^{-1}$ for TMC-*syn*. This energetic penalty might be related to the weak interactions between the bound $CH_3CN$ and the N-bound methyl groups in the TMC-*anti* ligand (in *syn* fashion with respect to $CH_3CN$). In the case of TMC-*syn*, these methyl groups are located on the opposite side of the ligand and hence have no such stabilizing interaction with $CH_3CN$. Therefore, the favorable HAT/OAT reactions with TMC-*syn*, and not TMC-*anti*, can be traced back to a combination of weak (dispersion) interactions that lower the energy of the σ* orbital as well as the dissociation of the axial $CH_3CN$ ligand.

These results reinforce the balance between stability and reactivity: The thermodynamically more stable Fe(IV)-oxo complex (TMC-*anti*) shows more favorable weak interactions with the axial ligand ($CH_3CN$), which disfavor HAT and OAT reactions compared to the kinetic Fe(IV)-oxo (TMC-*syn*) isomer. In the latter case, the axial ligand detaches from the metal center during the course of the OAT reaction, considerably enhancing the OAT reactivity of TMC-*syn*. This comparison of the two isomers suggests that the design of ligands for biomimetic oxidation chemistry may require a rethink when OAT reactions are targeted. Preferentially, the axial coordination site should be labile, allowing the metal-based oxidant to switch between pseudo-octahedral and square pyramidal symmetry for enhanced reactivity.

## Conclusions

Herein, we have described two topological isomers of $[Fe^{IV}(O)(TMC)(CH_3CN)]^{2+}$, TMC-*anti* and TMC-*syn*, that differ in the orientation of the $Fe^{IV}$=O moiety relative to the four methyl groups of the TMC ligand, resulting in differences in their oxidative reactivities. TMC-*syn* reacts with HAT substrates at 1.5- to 3-fold faster rates than TMC-*anti*. More strikingly, there is a much bigger difference in the OAT rates. $R_2S$ substrates are oxidized into $R_2S$=O products by TMC-*syn* at $10^2$- to $10^3$-fold faster rates than TMC-*anti*. Even more remarkably, TMC-*syn* epoxidizes all the olefin substrates examined in this study, while TMC-*anti* reacts only with *cis*-cyclooctene, the most electron-rich of the olefins studied here, but at a 100-fold slower rate than found for TMC-*syn*. Our DFT calculations show that the significant reactivity difference between the two Fe(O)TMC isomers derives from the 0.02 Å shorter Fe=O bond found for TMC-*syn*, the greater exposure of the TMC-*syn* Fe=O unit due to its larger out-of-plane distance from the TMC-N4 plane and the consequent longer distance of the *trans* axial $CH_3CN$ ligand that facilitates subsequent dissociation of $CH_3CN$ in the transition state to generate a much more reactive five-coordinate Fe(O)TMC oxidant in the course of substrate oxidation.

## Materials and Methods

A detailed *Experimental and Theoretical Methods* can be found in *SI Appendix*. These sections include detailed experimental procedures for the synthesis of our complexes, kinetic measurements, and product analysis, together with computational details, spin-resolved charge-displacement function, and definition of the out-of-plane distance. Additional figures and tables containing supporting data to the main text are also provided, including characterization of our complexes by UV–Vis and NMR spectroscopies, determination of kinetic measurements, cyclic voltammograms, GC–MS spectra, DFT-derived spin densities, and potential energy surfaces.

**Data, Materials, and Software Availability.** Computational data have been deposited in IOCHEM-BD (10.19061/iochem-bd-4-65) (49). All other data are included in the manuscript and/or *SI Appendix*.

**ACKNOWLEDGMENTS.** This work was supported by the NIH (grant R35 GM-131721 to L.Q.), AEI/MCIN (grant PID2020-114548GB-I00 to M.S.), GenCat (PhD fellowship 2022 FI_B 00118 and grant 2021SGR00487 to F.A.), and a developer's license to M.S. by SCM. We thankfully acknowledge the computer resources at Universidad de Málaga and the technical support provided by Picasso (QH-2023-1-0006). We thank Dr. Johannes Klein (University of Groningen) and Dr. Lorenzo D'Amore (Janssen Pharmaceuticals) for insightful discussions.

1. M. Costas, M. P. Mehn, M. P. Jensen, L. Que, Dioxygen activation at mononuclear nonheme iron active sites: Enzymes, models, and intermediates. *Chem. Rev.* **104**, 939–986 (2004).
2. A. J. Jasniewski, L. Que, Dioxygen activation by nonheme diiron enzymes: Diverse dioxygen adducts, high-valent intermediates, and related model complexes. *Chem. Rev.* **118**, 2554–2592 (2018).
3. M. Guo, T. Corona, K. Ray, W. Nam, Heme and nonheme high-valent iron and manganese oxo cores in biological and abiological oxidation reactions. *ACS Cent. Sci.* **5**, 13–28 (2019).
4. C. S. Abelson, A. M. Aboelenen, W. Rasheed, L. Que, "Synthetic nonheme high-valent iron-oxo complexes structures and oxidative function" in *Comprehensive Coordination Chemistry III* (Elsevier, 2021), pp. 412–454.
5. J.-U. Rohde *et al.*, Crystallographic and spectroscopic characterization of a nonheme Fe(IV)=O complex. *Science* **299**, 1037–1039 (2003).
6. W. Nam, Y.-M. Lee, S. Fukuzumi, Hydrogen atom transfer reactions of mononuclear nonheme metal-oxygen intermediates. *Acc. Chem. Res.* **51**, 2014–2022 (2018).
7. J. Li *et al.*, Epoxidation catalyzed by the nonheme iron(II)- and 2-oxoglutarate-dependent oxygenase, AsqJ: Mechanistic elucidation of oxygen atom transfer by a ferryl intermediate. *J. Am. Chem. Soc.* **142**, 6268–6284 (2020).
8. C. J. Thibodeaux, W. Chang, H. Liu, Enzymatic chemistry of cyclopropane, epoxide, and aziridine biosynthesis. *Chem. Rev.* **112**, 1681–1709 (2012).
9. M. A. Hollenhorst *et al.*, The nonribosomal peptide synthetase enzyme DdaD tethers $N_\beta$-fumaramoyl-L-2,3-diaminopropionate for Fe(II)/α-ketoglutarate-dependent epoxidation by DdaC during dapdiamide antibiotic biosynthesis. *J. Am. Chem. Soc.* **132**, 15773–15781 (2010).
10. V. Balland *et al.*, Spectroscopic characterization of an $Fe^{IV}$ intermediate generated by reaction of $XO^-$ (X = Cl, Br) with an $Fe^{II}$ complex bearing a pentadentate non-porphyrinic ligand—hydroxylation and epoxidation activity. *Eur. J. Inorg. Chem.* **2004**, 301–308 (2004).
11. J. Annaraj *et al.*, An iron(II) complex with a N3S2 thioether ligand in the generation of an iron(IV)-oxo complex and its reactivity in olefin epoxidation. *Inorg. Chim. Acta*. **362**, 1031–1034 (2009).
12. W. Ye, D. M. Ho, S. Friedle, T. D. Palluccio, E. V. Rybak-Akimova, Role of Fe(IV)-oxo intermediates in stoichiometric and catalytic oxidations mediated by iron pyridine-azamacrocycles. *Inorg. Chem.* **51**, 5006–5021 (2012).
13. S. H. Bae *et al.*, Mononuclear nonheme high-spin ($S = 2$) versus intermediate-spin ($S = 1$) iron(IV)–oxo complexes in oxidation reactions. *Angew Chem. Int. Ed.* **55**, 8027–8031 (2016).
14. J. P. Biswas *et al.*, Effect of the ligand backbone on the reactivity and mechanistic paradigm of non-heme iron(IV)-oxo during olefin epoxidation. *Angew. Chem. Int. Ed.* **60**, 14030–14039 (2021).
15. J. Prakash, G. T. Rohde, K. K. Meier, E. Münck, L. Que, Upside down! Crystallographic and spectroscopic characterization of an $[Fe^{IV}(O_{syn})(TMC)]^{2+}$ complex. *Inorg. Chem.* **54**, 11055–11057 (2015).
16. K. Ray *et al.*, An inverted and more oxidizing isomer of $[Fe^{IV}(O)(tmc)(NCCH_3)]^{2+}$. *Angew. Chem. Int. Ed.* **47**, 8068–8071 (2008).
17. R. Tyburski, T. Liu, S. D. Glover, L. Hammarström, Proton-coupled electron transfer guidelines, fair and square. *J. Am. Chem. Soc.* **143**, 560–576 (2021).
18. J. E. M. N. Klein, G. Knizia, cPCET versus HAT: A direct theoretical method for distinguishing X-H bond-activation mechanisms. *Angew. Chem. Int. Ed.* **57**, 11913–11917 (2018).
19. L. D'Amore, L. Belpassi, J. E. M. N. Klein, M. Swart, Spin-resolved charge displacement analysis as an intuitive tool for the evaluation of cPCET and HAT scenarios. *Chem. Commun.* **56**, 12146–12149 (2020).
20. J. England *et al.*, Oxoiron(IV) complex of the ethylene-bridged dialkylcyclam ligand $Me_2$EBC. *Inorg. Chem.* **54**, 7828–7839 (2015).
21. S. Grimme, J. Antony, S. Ehrlich, H. Krieg, A consistent and accurate *ab initio* parametrization of density functional dispersion correction (DFT-D) for the 94 elements H-Pu. *J. Chem. Phys.* **132**, 154104 (2010).

22. S. Grimme, Semiempirical GGA-type density functional constructed with a long-range dispersion correction. *J. Comput. Chem.* **27**, 1787–1799 (2006).
23. M. Swart, E. Rösler, F. M. Bickelhaupt, Proton affinities in water of maingroup-element hydrides–Effects of hydration and methyl substitution. *Eur. J. Inorg. Chem.* **2007**, 3646–3654 (2007).
24. A. Klamt, G. Schüürmann, COSMO: A new approach to dielectric screening in solvents with explicit expressions for the screening energy and its gradient. *J. Chem. Soc., Perkin Trans.* **2**, 799–805 (1993).
25. C. C. Pye, T. Ziegler, An implementation of the conductor-like screening model of solvation within the Amsterdam density functional package. *Theor. Chem. Acc.* **101**, 396–408 (1999).
26. E. V. Lenthe, E. J. Baerends, J. G. Snijders, Relativistic regular two-component Hamiltonians. *J. Chem. Phys.* **99**, 4597–4610 (1993).
27. M. L. Connolly, Solvent-accessible surfaces of proteins and nucleic acids. *Science* **221**, 709–713 (1983).
28. M. L. Neidig *et al.*, Spectroscopic and electronic structure studies of aromatic electrophilic attack and hydrogen-atom abstraction by non-heme iron enzymes. *Proc. Natl. Acad. Sci. U.S.A.* **103**, 12966–12973 (2006).
29. C. Geng, S. Ye, F. Neese, Analysis of reaction channels for alkane hydroxylation by nonheme iron(IV)–oxo complexes. *Angew. Chem. Int. Ed.* **49**, 5717–5720 (2010).
30. A. Kazaryan, E. J. Baerends, Ligand field effects and the high spin–high reactivity correlation in the H abstraction by non-heme iron(IV)–oxo complexes: A DFT frontier orbital perspective. *ACS Catal.* **5**, 1475–1488 (2015).
31. D. Schröder, S. Shaik, H. Schwarz, Two-state reactivity as a new concept in organometallic chemistry. *Acc. Chem. Res.* **33**, 139–145 (2000).
32. D. Usharani, B. Wang, D. A. Sharon, S. Shaik, "Principles and prospects of spin-states reactivity in chemistry and bioinorganic chemistry" in *Spin States in Biochemistry and Inorganic Chemistry*, M. Swart, M. Costas, Eds. (Wiley, 1st ed., 2015), pp. 131–156.
33. S. Shaik, S. P. De Visser, F. Ogliaro, H. Schwarz, D. Schröder, Two-state reactivity mechanisms of hydroxylation and epoxidation by cytochrome P-450 revealed by theory. *Curr. Opin. Chem. Biol.* **6**, 556–567 (2002).
34. L. Bernasconi, M. J. Louwerse, E. J. Baerends, The role of equatorial and axial ligands in promoting the activity of non-heme oxidoiron(IV) catalysts in alkane hydroxylation. *Eur. J. Inorg. Chem.* **2007**, 3023–3033 (2007).
35. D. Janardanan, D. Usharani, S. Shaik, The Origins of dramatic axial ligand effects: Closed-shell $Mn^{V}$ O complexes use exchange-enhanced open-shell states to mediate efficient H abstraction reactions. *Angew. Chem. Int. Ed.* **51**, 4421–4425 (2012).
36. J. T. Groves, Y. Watanabe, The mechanism of olefin epoxidation by oxo-iron porphyrins. Direct observation of an intermediate. *J. Am. Chem. Soc.* **108**, 507—508 (1986).
37. X. Engelmann *et al.*, Trapping of a highly reactive oxoiron(IV) complex in the catalytic epoxidation of olefins by hydrogen peroxide. *Angew. Chem. Int. Ed.* **58**, 4012–4016 (2019).
38. A. N. Biswas *et al.*, Modeling TauD-*J*: A high-spin nonheme oxoiron(IV) complex with high reactivity toward C-H bonds. *J. Am. Chem. Soc.* **137**, 2428–2431 (2015).
39. B. Wang, Y. Lee, M. S. Seo, W. Nam, Mononuclear nonheme iron(III)–iodosylarene and high-valent iron-oxo complexes in olefin epoxidation reactions. *Angew. Chem. Int. Ed.* **54**, 11740–11744 (2015).
40. S. N. Dhuri *et al.*, Interplay of experiment and theory in elucidating mechanisms of oxidation reactions by a nonheme $Ru^{IV}$ O Complex. *J. Am. Chem. Soc.* **137**, 8623–8632 (2015).
41. T. Terencio *et al.*, Chemoselectivity in the oxidation of cycloalkenes with a non-heme iron(IV)-oxo-chloride complex: Epoxidation vs. hydroxylation selectivity. *J. Am. Soc. Mass Spectrom.* **30**, 1923–1933 (2019).
42. M. Swart, PTh. Van Duijnen, J. G. Snijders, A charge analysis derived from an atomic multipole expansion. *J. Comput. Chem.* **22**, 79–88 (2001).
43. S. Hong *et al.*, Ligand topology effect on the reactivity of a mononuclear nonheme iron(IV)-oxo complex in oxygenation reactions. *J. Am. Chem. Soc.* **133**, 11876–11879 (2011).
44. D. Wang *et al.*, Nonheme oxoiron(IV) complexes of pentadentate N5 ligands: Spectroscopy, electrochemistry, and oxidative reactivity. *Chem. Sci.* **4**, 282–291 (2013).
45. Y.-M. Lee, H. Kotani, T. Suenobu, W. Nam, S. Fukuzumi, Fundamental electron-transfer properties of non-heme oxoiron(IV) complexes. *J. Am. Chem. Soc.* **130**, 434–435 (2008).
46. M. J. Bearpark, M. A. Robb, H. Bernhard Schlegel, A direct method for the location of the lowest energy point on a potential surface crossing. *Chem. Phys. Lett.* **223**, 269–274 (1994).
47. T. Takayanagi, T. Nakatomi, Automated reaction path searches for spin-forbidden reactions. *J. Comput. Chem.* **39**, 1319–1326 (2018).
48. J. N. Harvey, M. Aschi, H. Schwarz, W. Koch, The singlet and triplet states of phenyl cation. A hybrid approach for locating minimum energy crossing points between non-interacting potential energy surfaces. *Theor. Chem. Acc.* **99**, 95–99 (1998).
49. F. Ahsan, M. Swart, OAT_TP_KP collection. IOChem-BD. https://doi.org/10.19061/iochem-bd-4-65. Deposited 20 October 2023.